Elucidating microRNA-34a organisation within human Argonaute-2 by dynamic nuclear polarisation-enhanced magic angle spinning NMR

Rubin Dasgupta [1,2,†], Walter Becker[2,†] and Katja Petzold [1,2,3,4,*]

[1]Department of Medical Biochemistry and Microbiology, Uppsala University, Husargatan 3, 75237 Uppsala, Sweden
[2]Department of Medical Biochemistry and Biophysics, Karolinska Institute, 17177 Stockholm, Sweden
[3]Centre of Excellence for the Chemical Mechanisms of Life, Uppsala University, Husargatan 3, 75237 Uppsala, Sweden
[4]Science for Life Laboratory, Uppsala Biomedical Centre, Uppsala University, Husargatan 3, 75237 Uppsala, Sweden

[*]To whom correspondence should be addressed. Email: katja.petzold@imbim.uu.se
[†]The first two authors should be regarded as Joint First Authors.
Present address: Walter Becker, School of Chemistry, The University of Sydney, Sydney, New South Wales 2006, Australia.

Abstract

Understanding mRNA regulation by microRNA (miR) relies on the structural understanding of the RNA-induced silencing complex (RISC). Here, we elucidate the structural organisation of miR-34a, which is de-regulated in various cancers, in human Argonaute-2 (hAgo2), the effector protein in RISC. This analysis employs guanosine-specific isotopic labelling and dynamic nuclear polarisation (DNP)-enhanced Magic Angle Spinning (MAS) NMR. Homonuclear correlation experiments revealed that the non-A-form helical conformation of miR-34a increases when incorporated into hAgo2 and subsequently bound to SIRT1 mRNA compared to the free miR-34a or the free mRNA:miR duplex. The C8–C1′ correlation provided a nucleotide-specific distribution of C2′- and C3′-endo sugar puckering, revealing the capture of diverse dynamic conformations upon freezing. Predominantly C3′-endo puckering was observed for the seed region, while C2′-endo conformation was found in the central region, with a mixture of both conformations elsewhere. These observations provide insights into the molecular dynamics underlying miR-mediated mRNA regulation and demonstrate that experiments conducted under cryogenic conditions, such as at 90 K, can capture and reveal frozen dynamic states, using methods like DNP-enhanced MAS NMR or Cryo-Electron Microscopy.

Graphical abstract
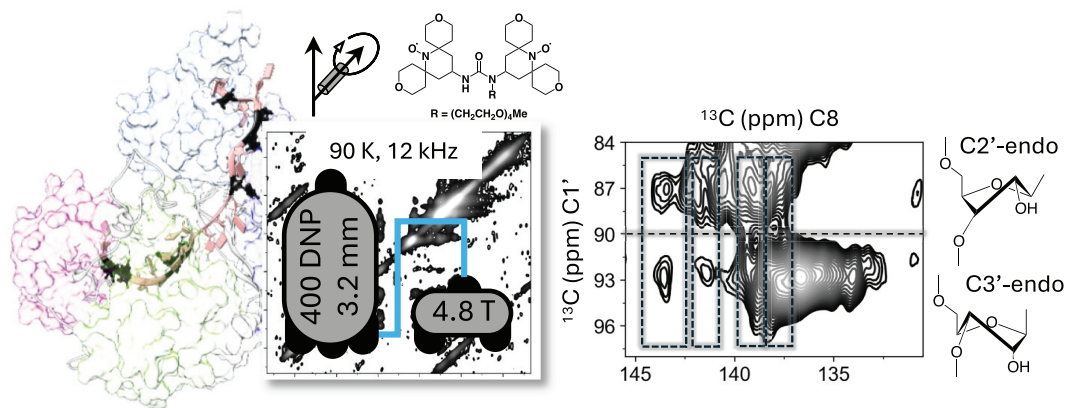
Introduction

MicroRNAs (miRs) are ∼22 nucleotide (nt) long RNAs that target messenger RNAs (mRNA) by binding the 3′-untranslated region (3′-UTR), and regulate these via the RNA-induced silencing complex (RISC) (1). miRs regulate more than half of all mRNAs and are regularly unbalanced in cancer and other diseases (2–5). The core of RISC consists of an Argonaute protein and a guide miR. Among the four isoforms of Argonaute proteins found in human, Argonaute-2 (hAgo2, EC:3.1.26.n2, 97 kDa) exhibits the highest miR-based target mRNA regulation and slicing activity (4,6,7). While X-ray crystal structures have provided key insights into its mechanism, a comprehensive structural model of miR in hAgo2 is lacking. This absence can be attributed to the ill-defined

electron densities of the miR's central region and partial densities in the overall 3′ region (Figure 1) (8–10) caused by the dynamic behaviour of the miR. Additionally, the weak electron densities complicate modelling the 3′ binding in both the presence and absence of the target mRNA (Figure 1). The central and the 3′ region of miR has recently been shown to be crucial for modulation of miR-based mRNA regulation (11,12).

Crystal structures (8–10,13–16) reveal that the seed region (nucleotide 2–8) of a miR is preorganised in a canonical A-form helix with the characteristic continuous C3′-endo ribose sugar pucker (Supplementary Table S1a,b and Figure 2). In absence of the mRNA target (hAgo2:miR, binary complex), the central, supplementary, and tail regions (nucleotides 9–12, 13–16 and 17–22 respectively) exhibit non-A-form conformations characterised by the mixture of both C3′- and C2′-endo ribose pucker (Supplementary Table S1a). In the presence of the mRNA target (ternary complex) (13–16), the central region remains dynamic with ill-defined electron density in the crystal structures, but the supplementary region adopts an A-form-like helical conformation with C3′-endo sugar pucker (Supplementary Table S1b) due to base paring with the mRNA.

Here, the structure and dynamics of miR-34a beyond the seed region using NMR spectroscopy is investigated. MiR-34a is directly regulated by tumour suppressor p53 (17), and down-regulated in >50% of tumours, indicating its biological importance. Via targeting the previously validated target mRNA encoding the deacetylase Sirtuin 1 (mSIRT1), miR-34a is involved in a feedback loop regulation of p53 (a gate keeper protein in cancer regulation) and itself (1,11,12,18,19). Understanding the regulation of SIRT1 by miR-34a has a potential for future cancer treatment (19). Additionally, several studies highlight the ability of miR-34a to inhibit Epithelial-to-Mesenchymal transition in cancer (20,21). Notably, miR-34a has been evaluated as a drug candidate against terminal liver cancer in a phase-I clinical trial with partial success (22), issues arising likely due to off-target effects. Enhancing the specificity of miR-34a requires detailed information of its structural organisation within hAgo2, which remains elusive at present. Here, miR-34a was investigated (a) in its isolated hairpin form, (b) as a duplex with a shortened 21nt construct of the 3′-UTR of mSIRT1, (c) in a binary complex with hAgo2 (104 kDa) and, (d) in a ternary complex with hAgo2 and mSIRT1 (110 kDa) (Figure 2A–D, Supplementary Tables S2–S4, Supplementary Figure S2).

Challenges in sample purification and preparation of the binary and ternary complex (18) limit the available sample quantity, making conventional NMR experiments, requiring millimolar concentration, unfeasible. Therefore, dynamic nuclear polarisation (DNP)-enhanced magic angle spinning (MAS) solid-state NMR was employed. In this technique, polarisation is transferred from unpaired electrons in a stable biradical to the nearby ^{1}H nuclei(23), providing necessary signal enhancement. MAS solid-state NMR has been previously utilised to study RNA and protein-RNA complexes (24–31), providing valuable insights into their structure. Recently, the Scream-DNP technique was developed to further enhance the study of long-range protein-RNA interactions (32) using direct polarisation of low gamma nuclei (^{13}C and ^{15}N). The cryo-temperatures (90–110 K) applied in DNP MAS NMR experiments result in reduced resolution and increased signal overlap. To address this resolution challenges,

^{13}C,^{15}N-guanosine-labelled miR-34a (G^{lab}-miR-34a) (33,34) representing all regions (seed nts 2, 3, 6 and 8; central nt 14; supplementary nt 17; tail nts 18 and 21) (4,35) was used (Figure 2A, B, D, Supplementary Figures S5–S6).

This study demonstrates an ∼200-fold signal enhancement factor using DNP, enabling comprehensive analysis of both binary and ternary complexes. This advancement provides insight into the structural organisation of the elusive central region and allows deeper insights into to the seed and the tail region of miR-34a within hAgo2. Additionally, it highlights the unique capability of DNP MAS NMR to trap and characterise low-populated dynamic states (usually present in equilibrium at room temperature) associated with ribose sugar puckering of miR-34a. This task is challenging for conventional structural biology techniques that also rely on cryogenic temperatures.

Materials and methods

RNA production and folding

miR-34a was produced from the tandem repeat plasmid reported previously (34) incorporating ^{13}C/^{15}N isotopically enriched guanosine. The 21nt SIRT1 target mRNA was produced using a single stranded DNA template annealed with the T7 promoter (Supplementary Table S2). The composition of the *in vitro* transcription reaction is shown in Supplementary Table S3. The RNAs were purified via denaturing polyacrylamide gel electrophoresis followed by extraction and ethanol precipitation (Supplementary Figure S1). miR-34a hairpin was folded by heating the buffered (NMR buffer: 15 mM NaP pH 6.5, 25 mM NaCl and 0.1 mM EDTA) solution to 95°C for 5 min followed by rapid cooling on ice for 20 min. The miR-34a–SIRT1 duplex was formed by heating the 1:1 mix to 95°C for 5 min followed by slow cooling to 25°C for 3 h.

Binary and ternary complex formation

hAgo2 was produced in insect cells from *Spodoptera frugiperda* (Sf9) using baculovirus generated from the pFast-Bac dual expression vector (Supplementary Figure S5). The purification of the protein was conducted following previously reported protocols (1,18). Subsequently, the protein was loaded with miR-34a to form the binary complex, and the integrity and concentration of the samples were assessed by comparative analysis of SDS PAGE, Western Blot, Bradford assay and Northern Blot, Furthermore, the activity of the protein was evaluated using slicing assay (Supplementary Table S4, Supplementary Figure S6). The ternary complex was formed by mixing the binary complex with 21nt SIRT1 mRNA and incubated for 1.5 h at 37°C.

NMR sample preparation and experiments

The hairpin and miR-34a:SIRT1 duplex were buffer exchanged to nuclease free water and was spiked with 9 μl of NMR buffer before lyophilizing. For the protein–RNA complex additional 175 mM trehalose and 329 mM mannitol was added as a cryoprotectant. The lyophilized power was reconstituted in 15 μl of ^{12}C, d$_8$-glycerol, 9 μl of nuclease free water containing 2 mM MgCl$_2$ and 1 μl of 300 mM AMUPol (giving a final concentration of 12 mM). The resulting solution of 25 μl was transferred into 3.2 mm sapphire rotor, sealed
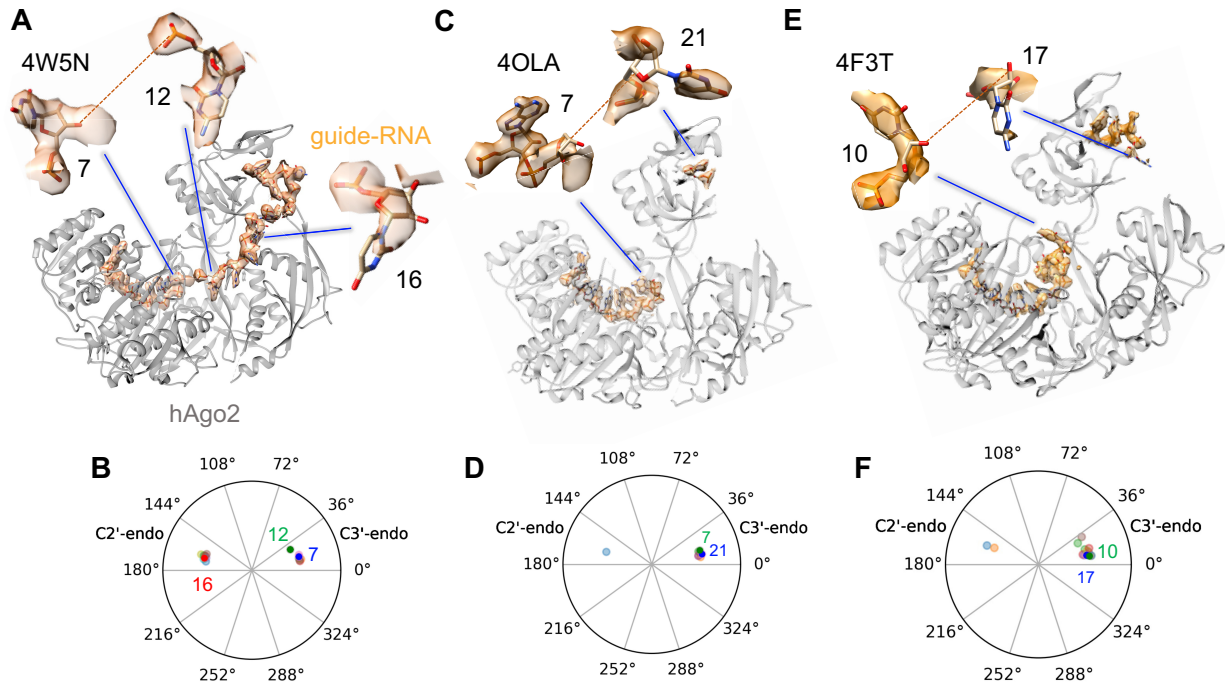
Figure 1. miR conformation within hAgo2 from crystal structures 4W5N (8) (**A**), 4OLA (9) (**C**) and 4F3T (10) (**E**) with protein ribbon in grey and RNA in sticks coloured according to atom type. The $2F_0 - F_c$ RNA electron density at 1σ of miR is shown in light orange. The dashed red line represents missing segments. Pseudo-rotation cycle corresponding to each crystal structure (panels **B**, **D** and **F**, respectively) shows the distribution of ribose C2'- and C3'-endo pucker. Nucleotides showing the partial electron density and with it the challenge of modelling ribose puckering and nucleobase orientation are shown above each crystal structures and numbered as in the pseudo-rotation cycles.
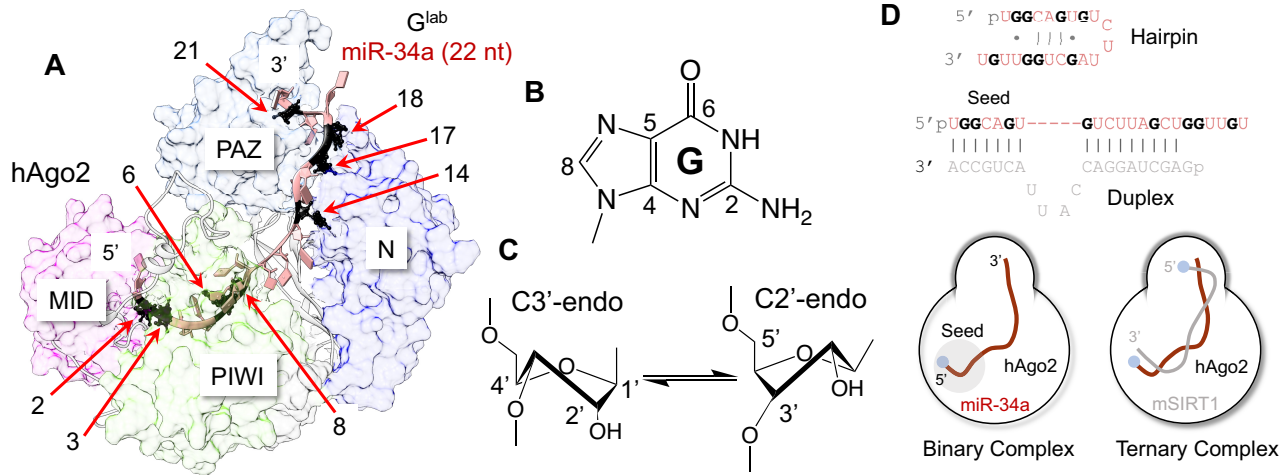

Figure 2. miR-34a in different complexes used in this study. (**A**) Model of hAgo2:miR-34a complex based on crystal structure 4W5N (8) depicting the four domains of the protein (MID pink, PIWI green, PAZ grey and N blue). Positions of $^{13}C/^{15}N$-labeled guanosines are denoted in black and numbered accordingly. (**B**) Chemical structure of guanosine nucleobase with carbons numbered. (**C**) Depiction of equilibrium between the C3'- and C2'-endo sugar puckering present in RNA. The ribose carbons are numbered in both C2'- and C3'-endo. (**D**) Overview of constructs used: top secondary structure (1) of miR-34a hairpin, next miR-34a:SIRT1(mRNA-grey) duplex, bottom schematic representation of the binary (left), and ternary (right) complexes. The seed region is highlighted in the duplex and binary complex. Labelled guanosines are indicated in bold. 5'-phosphate is shown as a blue circle in the binary and ternary complexes.

with a soft silicone plug and the drive cap for DNP MAS NMR.

DNP MAS NMR measurement was conducted using a 9.4 T magnet equipped with a 263 GHz gyrotron as the microwave source at 90 K with MAS of 12 kHz. Further experimental details can be found in the supporting information and Supplementary Table S5.

Molecular dynamic simulation

The binary complex was modelled using the crystal structure 4w5n (8) where the missing segment of the protein was modelled using SWISS-MODEL (36) and RNA using UCSF Chimera (37). Three different starting structures were simulated using GROMACS suite for 400 ns each amounting to a total simulation time of 1.2 μs. The trajectories were analysed

using UCSF Chimera (37) and in-house Python 3.08 script. Detailed simulation parameter, force field and python plugin information can be found in the supporting information.

Results and discussions

DNP MAS NMR was applied to reveal structural features of miR-34a alone and in different complexes, with the mRNA fragment of Sirt1, and with and without hAgo2. Specifically, ^{13}C cross-polarization (CP) (38), ^{13}C-^{31}P Transfer Echo Double Resonance (TEDOR) (39) and ^{13}C–^{13}C Dipolar Assisted Rotary Resonance (DARR) (40) experiments (Supplementary Table S5) were measured at 400.271 MHz ^{1}H Larmor frequency (9.4 T), 12 kHz MAS frequency at 90 K. Samples were dissolved in DNP solvent containing 60% ^{12}C,d$_8$-glycerol, 40% H$_2$O, 12 mM AMUPol (41), and for protein containing samples 175 mM of trehalose and 329 mM of mannitol were added as cryo-protectant (23,42–47). Trehalose and mannitol are commonly used to stabilize the proteins during lyophilisation (48,49); therefore, they were only added to the Ago containing samples. To ensure the comparability of spectra between RNA with and without protein, the hairpin miR-34a was titrated with varying concentrations of trehalose/mannitol solution. Supplementary Figure S1c demonstrates that the chemical shift of the imino resonances, indicative of the hairpin structure, remains unaffected by sugar concentration. Furthermore, to verify that the lyophilisation and the presence of sugars do not impact the activity of the binary complex, a slicing assay was conducted. Supplementary Figure S6e illustrates that the activity and structure of the active binary complex remains unchanged before lyophilisation without sugars and after lyophilisation with sugars.

The overall signal enhancement ($\varepsilon_{on/off}$, relative to the residual glycerol signal) observed is 220, 210, 230 and 210 for the hairpin, duplex, binary and ternary complex, respectively (Figure 3A, Supplementary Figures S2–S3a, S7–S8a), allowing the acquisition of homo- and heteronuclear correlation spectra from 1.45 nmol G^{lab}-miR-34a (60 μM in 25 μl of DNP solvent) in the binary and ternary complexes, respectively (Supplementary Table S5). It has been suggested that using deuterated trehalose could potentially improve $\varepsilon_{on/off}$ further (42,44,45), however, the current enhancement was adequate to obtained multidimensional experiments.

Using the 1D ^{13}C CP experiments, all carbons of guanosines (50) in the hairpin and duplex were detected (Figure 1e). Furthermore, for miR-34a in the binary and ternary complexes, carbonyl carbons, C$^{\gamma}$ of Asn or C$^{\delta}$ of Gln (165 – 185 ppm), ring carbons of Phe, Tyr, Trp or His (120–130 ppm) and aliphatic –C$^{\beta/\gamma}$ and –CH$_3$ carbons (12–42 ppm) (51) of the unlabelled hAgo2 were detectable (Figure 3A). DARR spectra with 250 ms mixing time show correlations between all carbons in the hairpin and duplex. However, resonance assignment was hindered by extensive overlap in other regions (Supplementary Figure S2c–d, S3c–d). This is likely due to signal broadening caused by freezing of multiple somewhat similar conformations and incomplete averaging of the chemical shift anisotropy (52,53). A similar overlap is observed in the binary and ternary complexes. However, the regions of C8–C1′ correlation exhibits higher resolution in the binary and ternary complexes compared to the hairpin and duplex samples. The resonance distribution of the C8–C1′ correlation from the DNP MAS NMR for the hairpin

and duplex RNA are consistent with the previously reported solution-state chemical shift (1) (Supplementary Figure S4), indicating that the RNA structure remains unaffected under DNP conditions. The discrepancy in absolute chemical shifts between the high-temperature solution-state and DNP conditions arises from the freezing of multiple conformational states of the RNA. This results in chemical shifts that differ from the ensemble-averaged chemical shift observed in the solution state, which is consistent with previous reports (52,53).

It is observed that for the binary and ternary complexes the C1′ resonances are split into two distinct regions (Figure 3B, Supplementary Figure S7c, d and S8c, d) and signals between 90.4 and 96.3 ppm can be attributed to C3′-endo sugar pucker with A-form helical conformation, while resonances between 86.6 and 90.0 ppm are associated to the C2′-endo sugar pucker with non A-form geometry (51,54–58). The positive projection of these regions from each of the systems studied shows that there is a 14.0 ± 0.2% and 11.3 ± 0.3% population of C2′-endo sugar pucker in the hairpin and duplex, respectively, based on Gaussian fits to the line shape. This increases to 34.4 ± 1% and 43.8 ± 1% for the binary and ternary complex, respectively, (Figure 4A–D, Supplementary Tables S6–S9) indicating that the protein stabilises the C2′-endo conformation more for certain guanosines. Furthermore indicating that the μs timescale dynamics of the sugar puckering (57) can be frozen into their respective ensembles and trapped for detection under DNP conditions. For the hairpin and duplex, the distribution of the C2′- and C3′-endo pucker in guanosines aligns with the population distribution previously reported for general helical nucleotides at room temperature (14%:88% for C2′:C3′-endo) (1,57). Additionally, low C2′-endo populations are confirmed by previous liquid-state study (1) of the hairpin and the duplex, that finds that the duplex is largely A-form like (Supplementary Figure S4). The appearance of distinct chemical shifts for these conformations suggests that the C2′- and C3′-endo conformational dynamics can be frozen trapped and studied under DNP conditions. The nucleotide specific distribution of these conformations provides crucial information for understanding of the structural organisation of different regions of G^{lab}-miR-34a. This is further explored using C8–C1′ correlations in the subsequent discussion (Figure 4).

Crystal structures of binary complexes (Supplementary Table S1a) suggest that nucleotides 2, 3, 6, 8 and 21 are in the C3′-endo conformation while nucleotides 14, 17 and 18 are in the C2′-endo conformation leading to a theoretical distribution of 62.5% (C3′-endo):37.5% (C2′-endo). This agrees with the fit of the regions in the DARR spectrum (Figure 4C) yielding a distribution of 65.6 ± 1% (C3′-endo):34.4 ± 1% (C2′-endo). In the ternary complex, the proportion of the C2′-endo increases to 43.8 ± 0.5% (Figure 4D). All the reported crystal structures (Supplementary Table S1b) of the ternary complex show that the nucleotides 2–8 of the guide RNA remain in the C3′-endo conformation, indicating that these nucleotides are not responsible for the increased proportion of C2′-endo conformation. Crystal structures 6N4O, 6NIT, 6MFR and 6MDZ (14,15) show that the central and supplementary regions exhibit a C3′-endo conformation in the presence of the mRNA target (Supplementary Table S1b). This contrasts our observation fitting the distribution of the DARR spectrum (Figure 4) obtained from the ternary complex. Interestingly, in the crystal structures 6NIT, 6MFR and 6MDZ (14), little to no interaction is observed between the RNA duplex with the
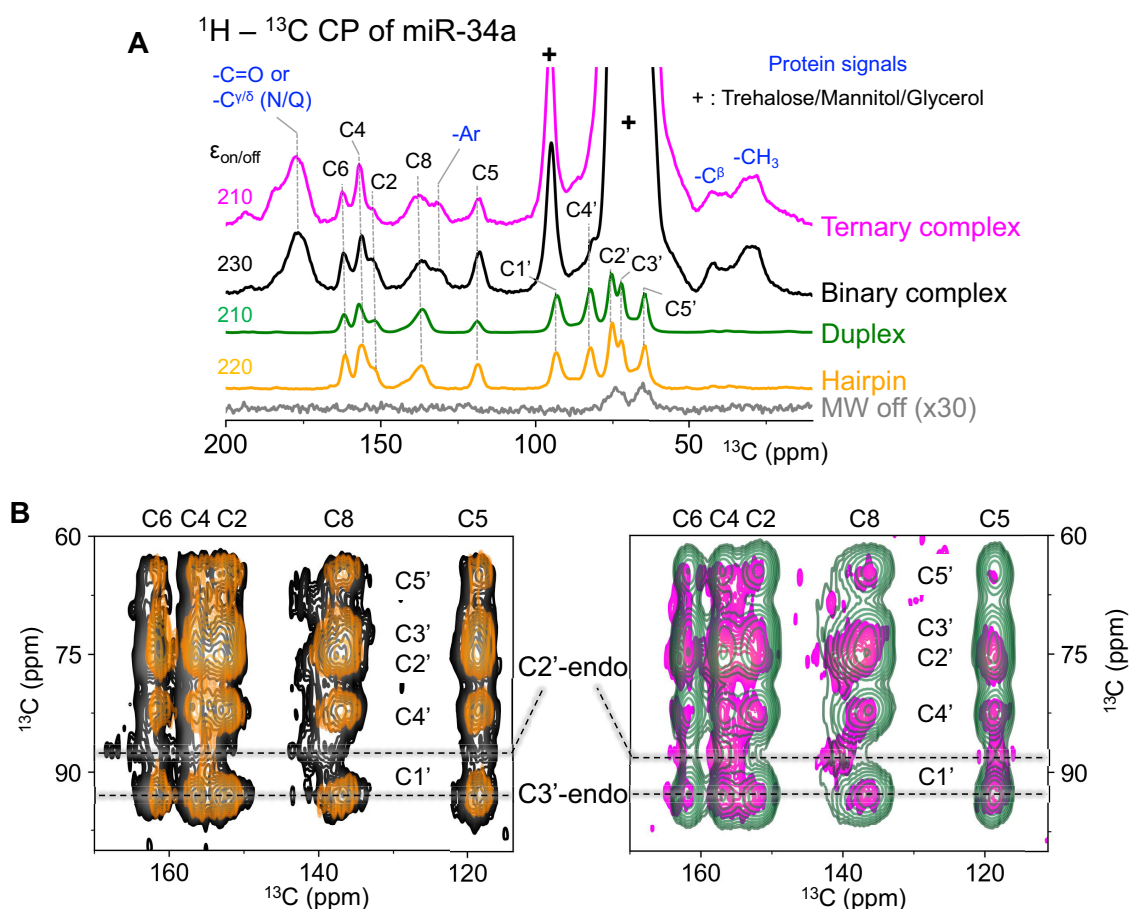
Figure 3. Strong signal enhancement reveals backbone dynamics. (**A**) 1D ^{13}C CP of G^{lab}-miR-34a as a hairpin (orange), in the duplex, (green), binary (black) and ternary (magenta) complexes. Microwave (MW) off condition is shown in grey, 30× enhanced. Signal from trehalose, mannitol and glycerol in the binary and ternary complex are indicated with ′+′. Signals from proteins are indicated in blue letters. Enhancement factor ($\varepsilon_{on/off}$) relative to the glycerol signal in the MW off condition is shown for each sample. (**B**) 2D ^{13}C–^{13}C DARR displaying correlations from the nucleobase (115–170 ppm) to ribose (60–100 ppm) carbons overlayed with lines at 93 ppm (C3′-endo) and 87 ppm (C2′-endo) C1′ chemical shifts indicating different populations in sugar puckers accessible in all complexes and the hairpin. The data indicates that the proportion of C2′-endo pucker of miR-34a increases with increasing complexity of the system.

PAZ domain of the protein, likely due to the RNA duplex release (11,14,15). In this study, optimisation of the experimental conditions mitigates duplex release from the protein by using a shortened 21nt target mRNA as previously reported (11,15,59–62). As 3 out 4 of ternary crystal structures experience release of the 3′ end miR, that allows for proper duplex formation, it is not surprising that the C3′-endo contribution is significantly higher as observed for the duplex sample here. While 6N4O, not releasing the 3′ miR end from the PAZ domain has a higher proportion of C2′-endo conformation in the 3′ supplementary region, although often found at other nucleotides, which can be correlated to the specific sequence.

In addition to revealing the overall puckering distribution (Figure 4A–D), the high-resolution in the C8–C1′ correlation region enabled a nucleotide-specific analysis of the puckering in the binary and ternary complexes. Gaussian peak fitting revealed 12 peaks for the binary complex and 11 peaks for the ternary complex across the entire C8 region of the eight guanosines. These additional resonances can originate from the changes around the glycosidic bond (χ-angle), to which the C8 chemical shift is sensitive. In the binary complex, seven resonances are exclusively in either conformation (4 C3′- and 3 C2′-endo), while four resonances showed a var-

ied distribution of 64:36%, 32:68%, 22:78% and 59:41% (error of <1%) for C2′:C3′-endo sugar puckering (Figure 4E and Supplementary Figure S9, Supplementary Table S10). The ternary complex exhibits less conformational diversity, with eight resonances remaining in a single conformation (4 C3′- and 4 C2′-endo), and three resonances displaying two conformations with distribution of 75:25%, 24:76% and 45:55% (error of <1%) (Figure 4E and Supplementary Figure S9, Supplementary Table S11). The ensemble-averaged chemical shift can be estimated from this population distribution, reflecting the high-temperature spectrum. However, to accurately predict the chemical shift at high temperatures, it is crucial to also consider the dynamics between the *syn-* and *anti-*conformations, in addition to the sugar puckering dynamics. The varied sugar puckering distributions indicate that each nucleotide has a different tendency to adopt C3′- (A-form) or C2′-endo (non-A-form) conformation, implying that cooling the sample does not favour the selection of a single conformation or promote a coalescing to the lowest energy conformation, as had been previously assumed (63). Additionally, the fact that the ternary complex spectrum does not collapse into the duplex spectrum (Figure 3b) demonstrates that duplex release is suppressed. It is acknowledged that the
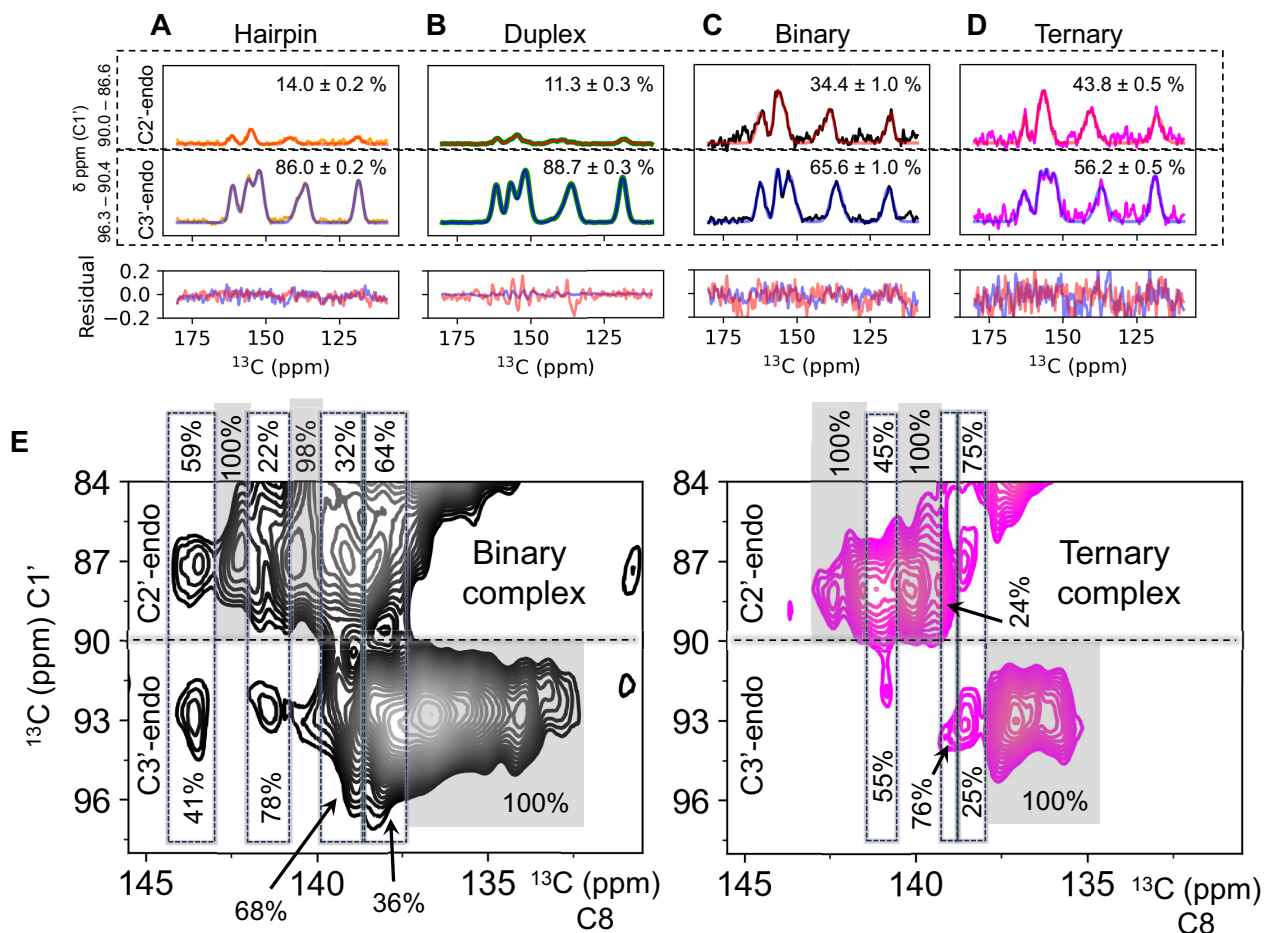
Figure 4. Dynamic analysis of the sugar pucker: Gaussian fits of the positive projection of the C1′ regions corresponding to C2′- (90.0 – 86.6 ppm) and C3′-endo (96.3 – 90.4 ppm) conformers from the DARR spectra of hairpin (orange, **A**), duplex (green, **B**), binary (black, **C**) and ternary (magenta, **D**) complex. Fits are red and blue solid lines, and residuals are shown for each sample together, data presented in Supplementary Table S6–S9. The chemical shift region used for the projection is denoted on the left side. The overall distribution in percent for each of the conformers is shown on the top right in the graph. The difference in noise level for different sample is due to different concentrations. The figure shows that the proportion of C2′-endo conformation of miR-34a increases within hAgo2 for both the binary and ternary complex. (**E**) Percentage distribution of C2′- and C3′-endo conformation after 2D deconvolution for the binary (black) and ternary (magenta) complex highlighting the capability of DNP MAS NMR to freeze the dynamic states. The guanosines exclusively present in either of the conformations are highlighted with grey boxes, while the box with dashed border shows guanosines with varying degree of mixed sugar puckers. Our data indicates the ability to extract nucleotide specific sugar puckering distribution by DNP MAS NMR, highlighting the ability to detect several conformations of one sugar being frozen in the solid state.

C2′- and C3′-endo puckering distribution might favour of C3′-endo in the ternary complex in the presence of a longer target RNA containing complementary partners for G17/18/21 (currently unpaired, as shown in Figure 2D) that may prompt these guanosines to adopt C3′-endo conformation. However, careful experimental design will be needed to address/find a fully bound target mRNA to the guide miR without duplex release.

To identify individual guanosines responsible for the different puckering signals, miR-34a was modelled into hAgo2 using crystal structure 4W5N (8) for the binary complex and simulated from three different starting structures for 400 ns each, totalling 1.2 µs. The puckering distribution showed that guanosines G2, G3 and G6 were exclusively in the C3′-endo, while G14 and G18 remained in the C2′-endo, and G8, G17 and G21 exhibited mixed conformations (Figure 5). Mapping this distribution onto the DARR region of C8–C1′ correlation from the binary complex, it can be hypothesized that resonances between 133 and 137 ppm with C3′-endo

conformation corresponds to G2/3/6. This aligns with reported crystal structures (Supplementary Table S1a), where the seed region is shown to be in the C3′-endo conformation. Signals between 140 and 141 ppm would then correspond to G14/18, while the signals with mixed C2′- and C3′-endo conformation could be attributed to G8/17/21. Under the assumptions made in the force field used for the MD simulations, a splitting of resonances due to trapped *anti* / *syn* conformations is likely to be found for G8, G14, G18 and G21 (Supplementary Figure S10), thereby explaining the increased number of resonances in the DARR deconvolution of the C8–C1′ correlation (Figure 4e and Supplementary Figure S9, Supplementary Table S10 and S11).

Interestingly, cross-peaks between the unlabelled hAgo2 (180–174 ppm) and G^{lab}-miR-34a (145–112 ppm), as well as intra-protein cross peaks, are readily observed in the binary complex (Figure 6A). These observations are enabled by a DARR mixing time of 250 ms, which can yield correlations between carbons of up to 6 Å apart (64). The MD

Different starting models for MD simulations
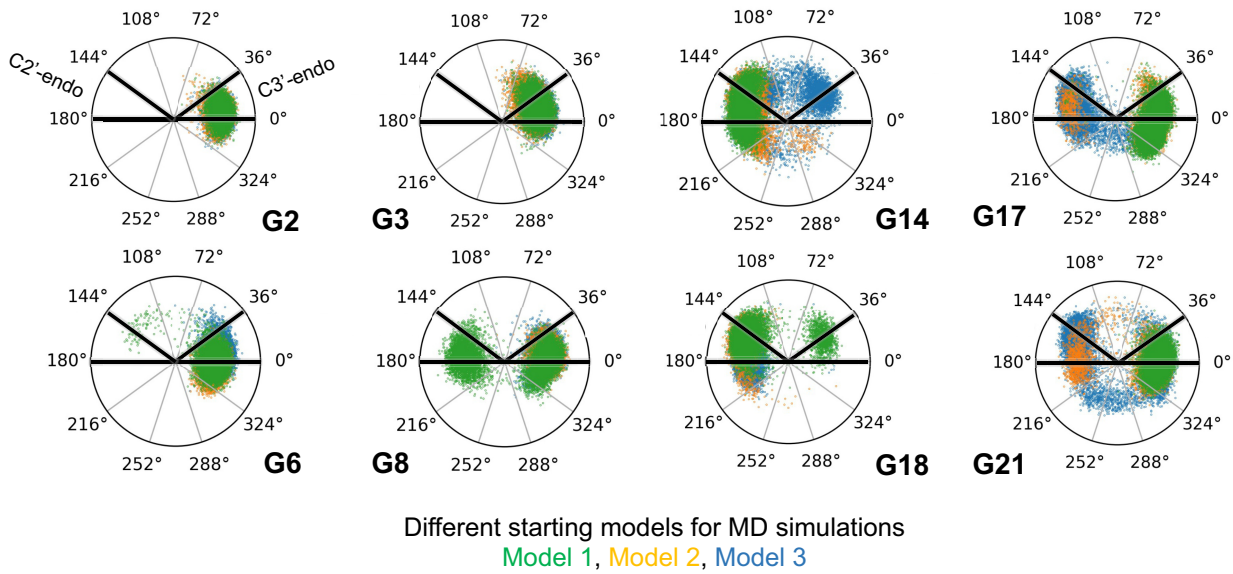Model 1, Model 2, Model 3

Figure 5. Sugar pucker distribution by MD: Ribose pucker pseudo rotation cycle indicating the distribution of each guanosine in miR-34a by MD simulation of the binary complex from three different starting models (blue, orange and green), C2′- and C3′-endo positions are denoted in G2. The observed sugar pucker distribution agrees well with the experimental observations.
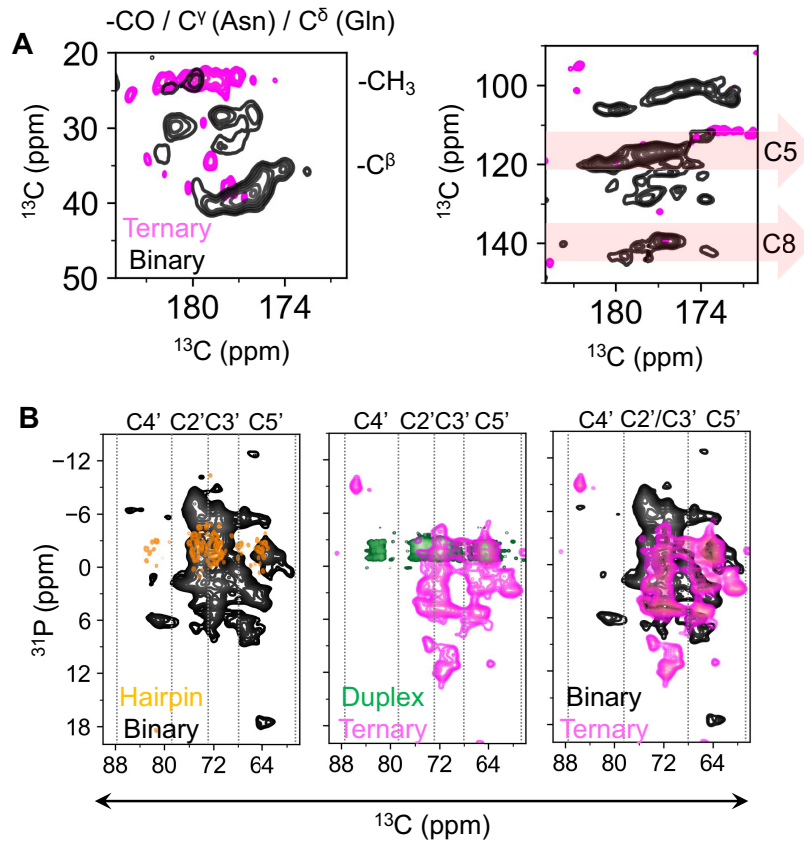

Figure 6. Observing contact with protein and changes in backbone. (**A**) DARR regions showing intra-hAgo2 cross-peaks of side chains (left panel) and inter hAgo2-G[lab]-miR-34a cross-peaks in binary and ternary complex (right panel), with C5 and C8 regions highlighted in red arrows. (**B**) Comparison of the ^{13}C-^{31}P TEDOR spectra from all the samples depicting the increased of spread of ^{31}P resonances in binary and ternary complexes compared to hairpin and duplex. Regions of ribose carbons indicated with dashed lines. Indicating here, that the miR-34a is strongly interacting with the protein, which in turns imposes a large variety of backbone conformations onto the RNA.

simulation trajectories were further analysed by (a) selecting amino-acids within a 6 Å zone around the guanosines of miR-34a and (b) comparing their carbon chemical shift with those in the Biological Magnetic Resonance Data Bank (BMRB). This analysis allowed the identification of DARR correlations to cross-peaks likely arising from Cys66 CO—G14C8, Asn551 C^{γ}—G2C5/C8 and Thr559 CO—G2C5/C8 (Figure 6A and Supplementary Figure S11). However, these cross-peaks were not observed in the hAgo2:G^{lab}-miR-34a:SIRT1 ternary complex (Figure 6B). Since there is no duplex release (Figure 6B middle, as explained above), this absence of cross-peaks is likely due to structural rearrangement imposed by the presence of the mRNA target. This rearrangement causes nucleobases of miR-34a to orient for base pair formation, supported by the chemical shift perturbations in the C8 to C5/6/4/2 correlations (Supplementary Figure S12). Consequently, the increased distance between the nucleobase carbons and the respective amino acids reduces the cross-peak intensity beyond detection.

Additional insights into the structural organisation of miR-34a in hAgo2 can be derived from ^{31}P chemical shifts along the RNA backbone. The 2D ^{31}P-^{13}C TEDOR spectra reveal that the ^{31}P resonances in the binary complex exhibit a significant increase in chemical shift dispersion of ∼16 ppm compared to ∼6 ppm in the hairpin (Figure 6B, Supplementary Figures S7e–S8e). The BMRB shows a typical spread of ∼8 ppm (−6 to 2 ppm from 74 entries as of February 2024 where two entries represent protein-RNA complex) for ^{31}P chemical shift of guanosines in RNA, which is increased compared to pure RNA structures but ultimately does not account for the current observation. Various factors can influence the ^{31}P chemical shift variation (65–70): Changes in A-form RNA alone do not explain the increased chemical shift spread; however, variations in backbone torsion angles or O–P–O bond angles might contribute to this phenomenon. Additionally, the observed chemical shift dispersion may result from a combination electrostatic potential and hydrophobicity within the protein binding pocket (Supplementary Figure S13). Furthermore, the similarity of the ^{31}P chemical shift dispersion between the binary and ternary complexes (Figure 6B) suggests that the RNA duplex remains stable within hAgo2, and the duplex release (15,60–62), even partially, is supressed, consistent with the above observations.

Conclusions

The application of DNP MAS NMR, with a signal enhancement of approximately 200, enabled the structural characterisation of the 104 kDa binary and 110 kDa ternary complex. This high signal enhancement facilitated the detection of correlations between G^{lab}-miR-34a and the unlabelled hAgo2, providing detailed insights into the conformational properties of miR-34a within RISC. The observed ^{31}P chemical shift dispersion and ribose pucker distribution indicate that the phenomenon of duplex release is supressed in the ternary complex. We were able to detect conformational ensembles being trapped in the frozen states, exhibiting varying distribution of the sugar pucker C2′- versus C3′-endo, demonstrating that DNP-enhanced solid-state NMR can monitor room temperature conformational heterogeneity under frozen conditions. Similar observations of frozen multiple conformations were made in DNP studies of proteins both *in vitro* and in cell (71), as well as in complementary cryo-EM studies (72,73). For large nucleic acids protein complexes, dynamic information typically being inferred from local disorder in crystal structure (B-factor) or the lack of defined electron density therein (8,9,15). Recent cryo-EM structure of plant Argonaute has shown two different conformations of the RNA duplex in the ternary complex, though detailed puckering information was not obtained due to low local resolution (74).

This study provides first observation of the different puckering preference of individual nucleotides in various regions of miR-34a, including the dynamic central region, which had not been observed in the crystal structures. It also highlights the capability of DNP MAS NMR to trap room temperature dynamic states, thereby providing structural information on low-populated states. Moreover, the presence of a 21nt SIRT1 target mRNA changes the conformational preferences and reduces the non-helicity of miR-34a by approximately 10%. This variation is expected to differ for other targets of miR-34a, opening possibilities for further studies of its conformation within hAgo2 in the presence of multiple targets. Ultimately, this could lead to a comprehensive understanding of miR-based target discrimination and regulation.

Data availability

All the NMR spectra, MD simulation models and gel images are provided in Zenodo, https://doi.org/10.5281/zenodo.12585837, and in the supplementary files.

Supplementary data

Supplementary Data are available at NAR Online.

Conflict of interest statement

None declared.

References

1. Baronti,L., Guzzetti,I., Ebrahimi,P., Friebe Sandoz,S., Steiner,E., Schlagnitweit,J., Fromm,B., Silva,L., Fontana,C., Chen,A.A., *et al.* (2020) Base-pair conformational switch modulates miR-34a targeting of Sirt1 mRNA. *Nature*, **583**, 139–144.

2. Wu,J., Yang,J., Cho,W.C. and Zheng,Y. (2020) Argonaute proteins: structural features, functions and emerging roles. *J. Adv. Res.*, **24**, 317–324.

3. Peng,Y. and Croce,C.M. (2016) The role of MicroRNAs in human cancer. *Sig. Transduct. Target Ther.*, **1**, 15004.

4. Iwakawa,H. and Tomari,Y. (2022) Life of RISC: formation, action, and degradation of RNA-induced silencing complex. *Mol. Cell*, **82**, 30–43.

5. Lessel,D., Zeitler,D.M., Reijnders,M.R.F., Kazantsev,A., Hassani Nia,F., Bartholomäus,A., Martens,V., Bruckmann,A., Graus,V., McConkie-Rosell,A., *et al.* (2020) Germline AGO2 mutations impair RNA interference and human neurological development. *Nat. Commun.*, **11**, 5797.

6. Meister,G., Landthaler,M., Patkaniowska,A., Dorsett,Y., Teng,G. and Tuschl,T. (2004) Human Argonaute2 mediates RNA cleavage targeted by miRNAs and siRNAs. *Mol. Cell*, **15**, 185–197.

7. Liu,J., Carmell,M.A., Rivas,F.V., Marsden,C.G., Thomson,J.M., Song,J.-J., Hammond,S.M., Joshua-Tor,L. and Hannon,G.J. (2004) Argonaute2 is the catalytic engine of mammalian RNAi. *Science*, **305**, 1437–1441.

8. Schirle,N.T., Sheu-Gruttadauria,J. and MacRae,I.J. (2014) Structural basis for microRNA targeting. *Science*, **346**, 608–613.

9. Schirle,N.T. and MacRae,I.J. (2012) The crystal structure of Human Argonaute2. *Science*, **336**, 1037–1040.

10. Elkayam,E., Kuhn,C.-D., Tocilj,A., Haase,A.D., Greene,E.M., Hannon,G.J. and Joshua-Tor,L. (2012) The structure of Human argonaute-2 in complex with miR-20a. *Cell*, **150**, 100–110.

11. Sweetapple,L., Kosek,D.M., Banijamali,E., Becker,W., Müller,J., Karadiakos,C., Baronti,L., Guzzetti,I., Schritt,D., Chen,A., *et al.* (2024) Biophysics of microRNA-34a targeting and its influence on down-regulation. bioRxiv doi: https://doi.org/10.1101/2024.02.14.580117, 16 February 2024, preprint: not peer reviewed.

12. Kosek,D.M., Banijamali,E., Becker,W., Petzold,K. and Andersson,E.R. (2023) Efficient 3′-pairing renders microRNA targeting less sensitive to mRNA seed accessibility. *Nucleic Acids Res.*, **51**, 11162–11177.

13. Schirle,N.T., Sheu-Gruttadauria,J., Chandradoss,S.D., Joo,C. and MacRae,I.J. (2015) Water-mediated recognition of t1-adenosine anchors Argonaute2 to microRNA targets. *eLife*, **4**, e07646.

14. Sheu-Gruttadauria,J., Pawlica,P., Klum,S.M., Wang,S., Yario,T.A., Schirle Oakdale,N.T., Steitz,J.A. and MacRae,I.J. (2019) Structural basis for target-directed MicroRNA degradation. *Mol. Cell*, **75**, 1243–1255.

15. Sheu-Gruttadauria,J., Xiao,Y., Gebert,L.F. and MacRae,I.J. (2019) Beyond the seed: structural basis for supplementary microRNA targeting by human Argonaute2. *EMBO J.*, **38**, e101153.

16. Gebert,L.F.R., Law,M. and MacRae,I.J. (2021) A structured RNA motif locks Argonaute2:miR-122 onto the 5′ end of the HCV genome. *Nat. Commun.*, **12**, 6836.

17. Hermeking,H. (2012) MicroRNAs in the p53 network: micromanagement of tumour suppression. *Nat. Rev. Cancer*, **12**, 613–626.

18. Banijamali,E., Baronti,L., Becker,W., Sajkowska-Kozielewicz,J.J., Huang,T., Palka,C., Kosek,D., Sweetapple,L., Müller,J., Stone,M.D., *et al.* (2023) RNA:RNA interaction in ternary complexes resolved by chemical probing. *RNA*, **29**, 317–329.

19. Yamakuchi,M., Ferlito,M. and Lowenstein,C.J. (2008) miR-34a repression of SIRT1 regulates apoptosis. *Proc. Natl. Acad. Sci. U.S.A.*, **105**, 13421–13426.

20. Siemens,H., Jackstadt,R., Hünten,S., Kaller,M., Menssen,A., Götz,U. and Hermeking,H. (2011) miR-34 and SNAIL form a double-negative feedback loop to regulate epithelial-mesenchymal transitions. *Cell Cycle*, **10**, 4256–4271.

21. Li,Z. and Chen,H. (2019) miR-34a inhibits proliferation, migration and invasion of paediatric neuroblastoma cells via targeting HNF4α. *Artif. Cells Nanomed. Biotechnol.*, **47**, 3072–3078.

22. Hong,D.S., Kang,Y.-K., Borad,M., Sachdev,J., Ejadi,S., Lim,H.Y., Brenner,A.J., Park,K., Lee,J.-L., Kim,T.-Y., *et al.* (2020) Phase 1 study of MRX34, a liposomal miR-34a mimic, in patients with advanced solid tumours. *Br. J. Cancer*, **122**, 1630–1637.

23. Chow,W.Y., De Paëpe,G. and Hediger,S. (2022) Biomolecular and biological applications of solid-State NMR with dynamic nuclear polarization enhancement. *Chem. Rev.*, **122**, 9795–9847.

24. Aguion,P.I., Marchanka,A. and Carlomagno,T. (2022) Nucleic acid–protein interfaces studied by MAS solid-state NMR spectroscopy. *J. Struct. Biol. X*, **6**, 100072.

25. Marchanka,A., Simon,B., Althoff-Ospelt,G. and Carlomagno,T. (2015) RNA structure determination by solid-state NMR spectroscopy. *Nat. Commun.*, **6**, 7024.

26. Marchanka,A., Simon,B. and Carlomagno,T. (2013) A suite of solid-State NMR experiments for RNA intranucleotide resonance assignment in a 21 kDa protein–RNA complex. *Angew. Chem. Int. Ed.*, **52**, 9996–10001.

27. Ahmed,M., Marchanka,A. and Carlomagno,T. (2020) Structure of a protein–RNA complex by solid-State NMR spectroscopy. *Angew. Chem.*, **132**, 6933–6940.

28. Huang,W., Varani,G. and Drobny,G.P. (2011) Interactions of protein side chains with RNA defined with REDOR solid state NMR. *J. Biomol. NMR*, **51**, 347–356.

29. Asami,S., Rakwalska-Bange,M., Carlomagno,T. and Reif,B. (2013) Protein–RNA interfaces probed by 1H-detected MAS solid-State NMR spectroscopy. *Angew. Chem. Int. Ed.*, **52**, 2345–2349.

30. Huang,W., Emani,P.S., Varani,G. and Drobny,G.P. (2017) Ultraslow domain motions in HIV-1 TAR RNA revealed by solid-State deuterium NMR. *J. Phys. Chem. B*, **121**, 110–117.

31. Olsen,G.L., Bardaro,M.F. Jr, Echodu,D.C., Drobny,G.P. and Varani,G. (2010) Intermediate rate atomic trajectories of RNA by solid-State NMR spectroscopy. *J. Am. Chem. Soc.*, **132**, 303–308.

32. Aladin,V., Sreemantula,A.K., Biedenbänder,T., Marchanka,A. and Corzilius,B. (2023) Specific signal enhancement on an RNA-protein interface by dynamic nuclear polarization. *Chemistry*, **29**, e202203443.

33. Karlsson,H., Baronti,L. and Petzold,K. (2020) A robust and versatile method for production and purification of large-scale RNA samples for structural biology. *RNA*, **26**, 1023–1037.

34. Feyrer,H., Munteanu,R., Baronti,L. and Petzold,K. (2020) One-pot production of RNA in high yield and purity through cleaving tandem transcripts. *Molecules*, **25**, 1142.

35. Bartel,D.P. (2009) MicroRNAs: target recognition and regulatory functions. *Cell*, **136**, 215–233.

36. Waterhouse,A., Bertoni,M., Bienert,S., Studer,G., Tauriello,G., Gumienny,R., Heer,F.T., de Beer,T.A.P., Rempfer,C., Bordoli,L., *et al.* (2018) SWISS-MODEL: homology modelling of protein structures and complexes. *Nucleic Acids Res.*, **46**, W296–W303.

37. Pettersen,E.F., Goddard,T.D., Huang,C.C., Couch,G.S., Greenblatt,D.M., Meng,E.C. and Ferrin,T.E. (2004) UCSF Chimera—A visualization system for exploratory research and analysis. *J. Comput. Chem.*, **25**, 1605–1612.

38. Levitt,M.H., Suter,D. and Ernst,R.R. (1986) Spin dynamics and thermodynamics in solid-state NMR cross polarization. *J. Chem. Phys.*, **84**, 4243–4255.

39. Jaroniec,C.P., Filip,C. and Griffin,R.G. (2002) 3D TEDOR NMR experiments for the simultaneous measurement of multiple carbon−nitrogen distances in uniformly 13C,15N-labeled solids. *J. Am. Chem. Soc.*, **124**, 10728–10742.

40. Takegoshi,K., Nakamura,S. and Terao,T. (2001) 13C–1H dipolar-assisted rotational resonance in magic-angle spinning NMR. *Chem. Phys. Lett.*, **344**, 631–637.

41. Sauvée,C., Rosay,M., Casano,G., Aussenac,F., Weber,R.T., Ouari,O. and Tordo,P. (2013) Highly efficient, water-soluble

polarizing agents for dynamic nuclear polarization at high frequency. *Angew. Chem. Int. Ed.*, **52**, 10858–10861.

42. Gauto,D., Dakhlaoui,O., Marin-Montesinos,I., Hediger,S. and Paëpe,G.D. (2021) Targeted DNP for biomolecular solid-state NMR. *Chem. Sci.*, **12**, 6223–6237.

43. Conroy,D.W., Xu,Y., Shi,H., Gonzalez Salguero,N., Purusottam,R.N., Shannon,M.D., Al-Hashimi,H.M. and Jaroniec,C.P. (2022) Probing Watson-Crick and Hoogsteen base pairing in duplex DNA using dynamic nuclear polarization solid-state NMR spectroscopy. *Proc. Natl. Acad. Sci. U.S.A.*, **119**, e2200681119.

44. Brender,J.R., Kishimoto,S., Eaton,G.R., Eaton,S.S., Saida,Y., Mitchell,J. and Krishna,M.C. (2021) Trehalose as an alternative to glycerol as a glassing agent for in vivo DNP MRI. *Magn. Reson. Med.*, **85**, 42–48.

45. Kaushik,M., Lingua,H., Stevanato,G., Elokova,M., Lelli,M., Lesage,A. and Ouari,O. (2022) Trehalose matrices for high temperature dynamic nuclear polarization enhanced solid state NMR. *Phys. Chem. Chem. Phys.*, **24**, 12167–12175.

46. Fernández-de-Alba,C., Takahashi,H., Richard,A., Chenavier,Y., Dubois,L., Maurel,V., Lee,D., Hediger,S. and De Paëpe,G. (2015) Matrix-free DNP-enhanced NMR spectroscopy of liposomes using a lipid-anchored biradical. *Chemistry*, **21**, 4512–4517.

47. Takahashi,H., Hediger,S. and Paëpe,G.D. (2013) Matrix-free dynamic nuclear polarization enables solid-state NMR 13C–13C correlation spectroscopy of proteins at natural isotopic abundance. *Chem. Commun.*, **49**, 9479–9481.

48. Sonje,J., Chisholm,C.F. and Suryanarayanan,R. (2023) Frozen storage of proteins: use of mannitol to generate a homogenous freeze-concentrate. *Int. J. Pharm.*, **630**, 121995.

49. Jain,N.K. and Roy,I. (2010) Trehalose and protein stability. *Curr. Prot. Protein Sci.*, **59**, 4.9.1–4.9.12.

50. Marchanka,A. and Carlomagno,T. (2019) Chapter nine - solid-State NMR spectroscopy of RNA. In: Wand,A.J. (ed.) *Methods in Enzymology, Biological NMR Part B*. Academic Press, Vol. **615**, pp. 333–371.

51. Hoch,J.C., Baskaran,K., Burr,H., Chin,J., Eghbalnia,H.R., Fujiwara,T., Gryk,M.R., Iwata,T., Kojima,C., Kurisu,G., *et al.* (2023) Biological magnetic resonance data bank. *Nucleic Acids Res.*, **51**, D368–D376.

52. Kragelj,J., Dumarieh,R., Xiao,Y. and Frederick,K.K. (2023) Conformational ensembles explain NMR spectra of frozen intrinsically disordered proteins. *Protein Sci.*, **32**, e4628.

53. Yi,X., Zhang,L., Friesner,R.A. and McDermott,A. (2024) Predicted and experimental NMR chemical shifts at variable temperatures: the effect of protein conformational dynamics. *J. Phys. Chem. Lett.*, **15**, 2270–2278.

54. Aeschbacher,T., Schubert,M. and Allain,F.H.-T. (2012) A procedure to validate and correct the 13C chemical shift calibration of RNA datasets. *J. Biomol. NMR*, **52**, 179–190.

55. Xu,X.-P. and Au−Yeung,S.C.F. (2000) Investigation of chemical shift and structure relationships in nucleic acids using NMR and density functional theory methods. *J. Phys. Chem. B*, **104**, 5641–5650.

56. Dejaegere,A.P. and Case,D.A. (1998) Density functional study of ribose and deoxyribose chemical shifts. *J. Phys. Chem. A*, **102**, 5280–5289.

57. Clay,M.C., Ganser,L.R., Merriman,D.K. and Al-Hashimi,H.M. (2017) Resolving sugar puckers in RNA excited states exposes slow modes of repuckering dynamics. *Nucleic Acids Res.*, **45**, e134.

58. Richardson,J.S., Schneider,B., Murray,L.W., Kapral,G.J., Immormino,R.M., Headd,J.J., Richardson,D.C., Ham,D., Hershkovits,E., Williams,L.D., *et al.* (2008) RNA backbone: consensus all-angle conformers and modular string nomenclature (an RNA Ontology Consortium contribution). *RNA*, **14**, 465–481.

59. Wang,P.Y. and Bartel,D.P. (2024) The guide-RNA sequence dictates the slicing kinetics and conformational dynamics of the Argonaute silencing complex. *Mol. Cell*, **84**, 2918–2934.

60. De,N., Young,L., Lau,P.-W., Meisner,N.-C., Morrissey,D.V. and MacRae,I.J. (2013) Highly complementary target RNAs promote release of guide RNAs from Human Argonaute2. *Mol. Cell*, **50**, 344–355.

61. Jo,M.H., Shin,S., Jung,S.-R., Kim,E., Song,J.-J. and Hohng,S. (2015) Human Argonaute 2 has diverse reaction pathways on target RNAs. *Mol. Cell*, **59**, 117–124.

62. Park,J.H., Shin,S.-Y. and Shin,C. (2017) Non-canonical targets destabilize microRNAs in human Argonautes. *Nucleic Acids Res.*, **45**, 1569–1583.

63. Bock,L.V. and Grubmüller,H. (2022) Effects of cryo-EM cooling on structural ensembles. *Nat. Commun.*, **13**, 1709.

64. Loquet,A., Bardiaux,B., Gardiennet,C., Blanchet,C., Baldus,M., Nilges,M., Malliavin,T. and Böckmann,A. (2008) 3D Structure determination of the crh protein from highly ambiguous solid-State NMR restraints. *J. Am. Chem. Soc.*, **130**, 3579–3589.

65. Castagné,C., Murphy,E.C., Gronenborn,A.M. and Delepierre,M. (2000) 31P NMR analysis of the DNA conformation induced by protein binding. *Eur. J. Biochem.*, **267**, 1223–1229.

66. Gorenstein,D.G., Karslake,C., Granger,J.N., Cho,Y. and Piotto,M.E. (1992) DNA—The ultimate phosphorus polymer. In: *Phosphorus Chemistry*. ACS Symposium Series. American Chemical Society, Vol. **486**, pp. 202–217.

67. Gorenstein,D.G. (1975) Dependence of phosphorus-31 chemical shifts on oxygen-phosphorus-oxygen bond angles in phosphate esters. *J. Am. Chem. Soc.*, **97**, 898–900.

68. Prado,F.R., Giessner-Prettre,C., Pullman,B. and Daudey,J.P. (1979) Ab initio quantum mechanical calculations of the magnetic shielding tensor of phosphorus-31 of the phosphate group. *J. Am. Chem. Soc.*, **101**, 1737–1742.

69. Giessner-Prettre,C., Pullman,B., Parado,F.R., Cheng,D.M., Iuorno,V. and Ts'O,P.O.P. (1984) Contributions of the PO ester and CO torsion angles of the phosphate group to 31P-nuclear magnetic shielding constant in nucleic acids: theoretical and experimental study of model compounds. *Biopolymers*, **23**, 377–388.

70. Gorenstein,D.G. (1984) Introduction. In: Gorenstein,D.G. (ed.) *Phosphorous-31 NMR*. Academic Press, San Diego, pp. 1–4.

71. Beriashvili,D., Yao,R., D'Amico,F., Krafčíková,M., Gurinov,A., Safeer,A., Cai,X., Mulder,M.P.C., Liu,Y., Folkers,G.E., *et al.* (2023) A high-field cellular DNP-supported solid-state NMR approach to study proteins with sub-cellular specificity. *Chem. Sci.*, **14**, 9892–9899.

72. Geraets,J.A., Pothula,K.R. and Schröder,G.F. (2020) Integrating cryo-EM and NMR data. *Curr. Opin. Struct. Biol.*, **61**, 173–181.

73. Gremer,L., Schölzel,D., Schenk,C., Reinartz,E., Labahn,J., Ravelli,R.B.G., Tusche,M., Lopez-Iglesias,C., Hoyer,W., Heise,H., *et al.* (2017) Fibril structure of amyloid-β(1–42) by cryo–electron microscopy. *Science*, **358**, 116–119.

74. Xiao,Y., Maeda,S., Otomo,T. and MacRae,I.J. (2023) Structural basis for RNA slicing by a plant Argonaute. *Nat. Struct. Mol. Biol.*, **30**, 778–784.